Supplementary Materials

Room Temperature Optically and Magnetically Active Edges in Phosphorene Nanoribbons

[1]Arjun Ashoka, [2,3]Adam J. Clancy[#], [4]Naitik A. Panjwani[#], [1]Nicholas J. M. Popiel, [1]Alex Eaton, [5]Thomas G. Parton, [6]Loren Picco, [1] Sascha Feldmann, [3]Rebecca R. C. Shutt, [1]Remington Carey, [3]Eva S. Y. Aw, [2,7,8]Thomas J. Macdonald, [9] Marion E. Severijnen, [9]Sandra Kleuskens, [10]Hilton Barbosa de Aguiar, [1]Richard H. Friend, [4]Jan Behrends, [9] Peter C.M. Christianen, [3]Christopher A. Howard, [1]Akshay Rao and [1,10]Raj Pandya✉

[1]Cavendish Laboratory, University of Cambridge, J.J. Thomson Avenue, CB3 0HE, Cambridge, United Kingdom
[2]Department of Chemistry, UCL, Christopher Ingold Building, Gordon St, London WC1H 0AJ, UK
[3]Department of Physics & Astronomy, University College London, London, WC1E 6BT, United Kingdom
[4]Berlin Joint EPR Lab, Fachbereich Physik, Freie Universität Berlin, D-14195 Berlin, Germany
[5]Yusuf Hamied Department of Chemistry, University of Cambridge, Lensfield Road, Cambridge, CB2 1EW, United Kingdom
[6]Department of Physics, Virginia Commonwealth University, Richmond, VA, USA
[7]Department of Chemistry and Centre for Processable Electronics, Imperial College London, London, W12 0BZ, United Kingdom
[8]School of Engineering and Materials Science, Queen Mary University of London, London E1 4NS, United Kingdom
[9]High Field Magnet Laboratory (HFML - EMFL), Radboud University, 6525 ED, Nijmegen, The Netherlands
[10]Laboratoire Kastler Brossel, ENS-Université PSL, CNRS, Sorbonne Université, Collège de France, 24 rue Lhomond, 75005, Paris, France

#Denotes equal contribution
Correspondence: rp558@cam.ac.uk

Contents

Supplementary Note 1: Calculation of volume susceptibility

For both diamagnetism and paramagnetism the magnetic moment induced by an external magnetic field $\boldsymbol{B}$ is given by,

$$\boldsymbol{m} = \frac{\boldsymbol{\chi V}}{\boldsymbol{\mu_0}} \cdot \boldsymbol{B}$$

The magnetic interaction energy is given as the projection of the magnetic moment along the applied field direction, *i.e.*,

$$\boldsymbol{E(B)} = -\int_0^{\boldsymbol{B}} \boldsymbol{m} \cdot \boldsymbol{dB} = -\frac{\boldsymbol{\chi V}}{\boldsymbol{2\mu_0}} \boldsymbol{B^2}$$

Where $\chi \approx 10^{-3}$ with χ positive for paramagnetism and $\chi \approx -10^{-5}$, χ negative for diamagnetism. For a magnetically anisotropic material with in-plane isotropy, χ can be represented as,

$$\boldsymbol{\chi} = \begin{pmatrix} \boldsymbol{\chi_\perp} & \boldsymbol{0} & \boldsymbol{0} \\ \boldsymbol{0} & \boldsymbol{\chi_{||}} & \boldsymbol{0} \\ \boldsymbol{0} & \boldsymbol{0} & \boldsymbol{\chi_{||}} \end{pmatrix}$$

The magnetic moment and energy along the two directions are therefore

$$\begin{cases} \boldsymbol{m_\perp} = \frac{\boldsymbol{\chi_\perp V \cdot B}}{\boldsymbol{\mu_0}} & \Rightarrow \quad \boldsymbol{E} = -\frac{\boldsymbol{\chi_\perp V}}{\boldsymbol{2\mu_0}} \boldsymbol{B^2} \\ \boldsymbol{m_{||}} = \frac{\boldsymbol{\chi_{||} V \cdot B}}{\boldsymbol{\mu_0}} & \Rightarrow \quad \boldsymbol{E} = -\frac{\boldsymbol{\chi_{||} V}}{\boldsymbol{2\mu_0}} \boldsymbol{B^2} \end{cases}$$

There is therefore an energy associated with the anisotropy of the magnetic susceptibility χ called the orientational anisotropy energy,

$$\boldsymbol{\Delta E_{an}} = -\frac{(\boldsymbol{\chi_{||} - \chi_\perp})\boldsymbol{V}}{\boldsymbol{2\mu_0}} \boldsymbol{B^2} = -\frac{\boldsymbol{\Delta \chi V}}{\boldsymbol{2\mu_0}} \boldsymbol{B^2}.$$

For a material with optical anisotropy measured through the magnetic birefringence, the birefringence is assumed to measure the degree of alignment $\boldsymbol{S}$,

$$\boldsymbol{S} = \frac{\boldsymbol{3 \cdot \langle \cos^2 \theta \rangle - 1}}{\boldsymbol{2}}$$

where,

$\langle \cos^2 \boldsymbol{\theta} \rangle = \frac{\int \cos^2 \boldsymbol{\theta} \cdot \boldsymbol{f(\theta)} \cdot \sin \boldsymbol{\theta} \cdot \boldsymbol{d\theta}}{\int \boldsymbol{f(\theta)} \cdot \sin \boldsymbol{\theta} \cdot \boldsymbol{d\theta}}$ and $\langle \cos^2 \boldsymbol{\theta} \rangle = \frac{\int \cos^2 \boldsymbol{\theta} \cdot \boldsymbol{f(\theta)} \cdot \sin \boldsymbol{\theta} \cdot \boldsymbol{d\theta}}{\int \boldsymbol{f(\theta)} \cdot \sin \boldsymbol{\theta} \cdot \boldsymbol{d\theta}}$.

Hence by fitting the magnetic birefringence as a function of applied field, we are able to determine the volume susceptibility $\boldsymbol{\chi_V}$. Further the field required to align the PNRs at room temperature depends on the volume of the PNRs,

$$\frac{\Delta \chi V}{2\mu_0} B^2 \geq k_B T$$

Supplementary Note 2: Additional SQUID magnetometry measurements

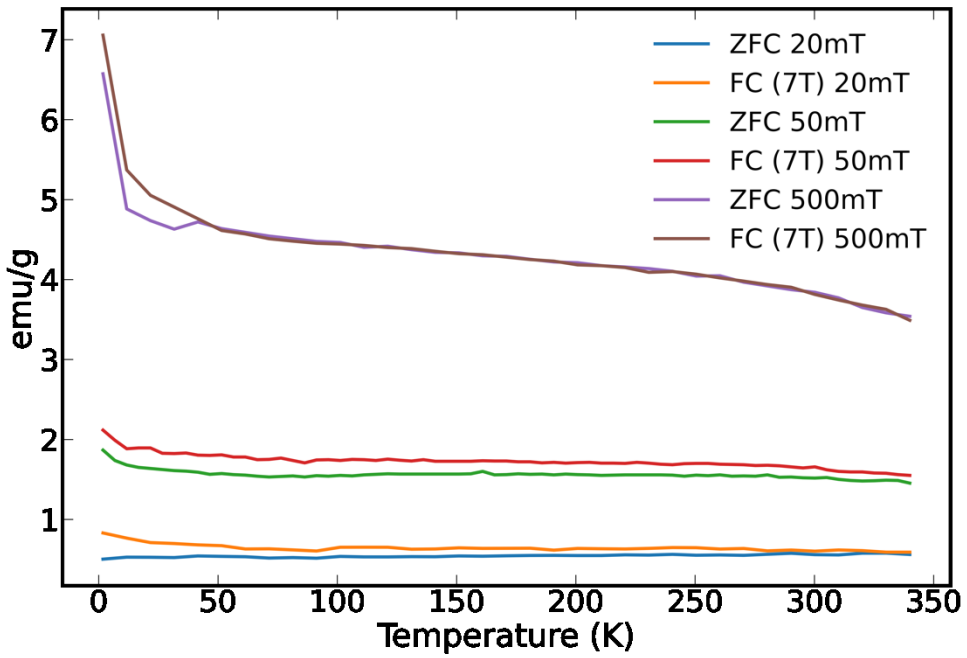

Fig. S1: Field and Zero Field Cooled Magnetization as a function of projecting field: Zero field (ZFC) and Field cooled (FC) at 7T magnetization measured in different projecting fields to demonstrate the sensitivity of the PNRs to the projecting field. If the projecting field is above the coercive field (>50 mT), the room temperature magnetic phase ceases to exist, likely due to the projecting field polarizing all the spins during the measurement. At 50 mT and 20 mT however, it can be seen that the ZFC and FC begin to approach each other towards room temperature but do not yet overlap, signifying that the room temperature magnetic phase can only be measured with very low projecting fields.

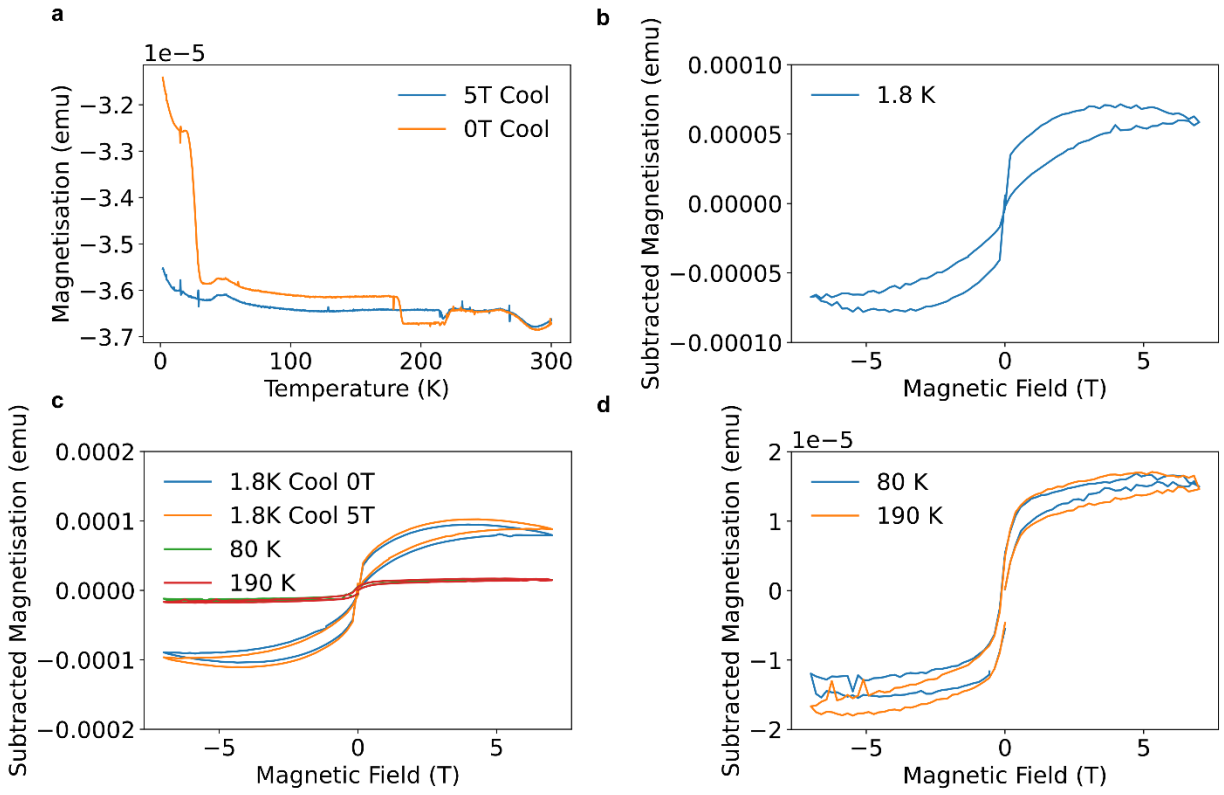

Fig. S2: SQUID measurement of PNRs in solution (DMF and NMP): a-d. In both DMF (a-b) and NMP (c-d) below the freezing point (220 K) as the thermal motion of the ribbons in solution is frozen out, it can be seen that the PNRs in solution begin to behave as the solid state PNRs reported in the main text – displaying both hysteresis in the isothermal magnetization sweeps and field and zero field cooled magnetization sweeps that are split up to the freezing point of the solvent.

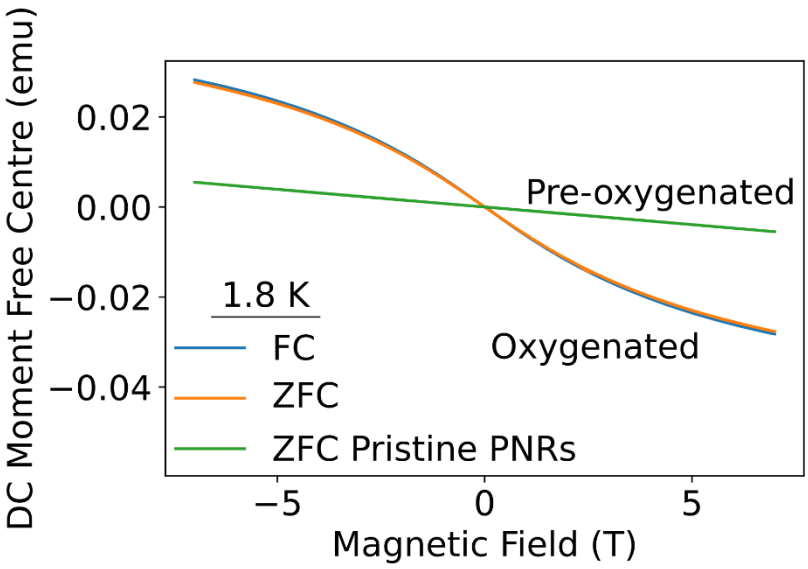

Fig. S3: Increased diamagnetic background after exposure of PNRs to air: Upon exposure to air in the diamagnetic background of the PNRs can be seen to increase. This diamagnetic background in the un-oxygenated scenario arises from the solvent and is subtracted by fitting the high field limits to straight lines to retrieve the PNRs behavior.

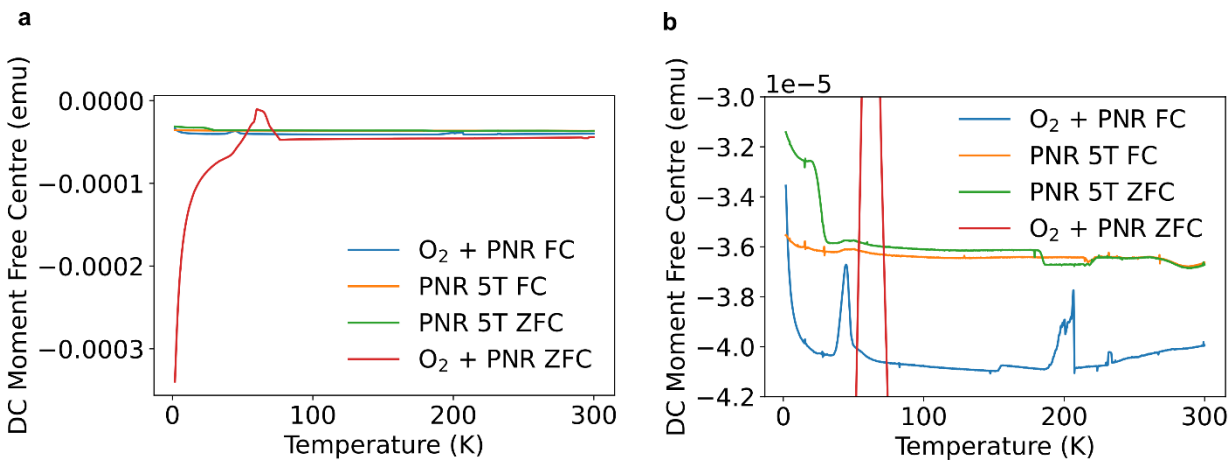

Fig. S4: SQUID measurement of PNRs in solution before and after exposure to air after subtraction: a-b. The magnetic behavior after subtracting the increased diamagnetic background is also increased suggesting that the magnetic behavior of the PNRs themselves has been altered and the rise in the background diamagnetism likely comes from the reacted PNRs. Figure b is a zoom in on a.

Supplementary Note 3: Elemental Analysis of the PNR solution (ICP-OES)

	Fe (ppb)	Ni (ppb)	Co (ppb)	Cr (ppb)	Mn (ppb)
2D semiconductors PNRs in NMP	10.1	0.2	<0.1	<0.1	<0.1
Smart Materials – PNRS in NMP	8	0.2	<0.1	<0.1	<0.1
Smart Materials PNRs in DMF	5	0.2	<0.1	<0.1	<0.1
DMF solvent	6	0.4	<0.1	<0.1	<0.1
NMP solvent	7	0.2	<0.1	<0.1	<0.1
LiP_8	6.4	0.2	<0.1	<0.1	<0.1
2D semiconductors Black Phosphorous	1.75	0.14	<0.1	<0.1	<0.1

Table S1: Results of the Inductively Coupled Plasma Optical Emission Spectroscopy (ICP-OES) on the PNR solution: ICP-OES of PNRs made from two different black phosphorous precursors (2D semiconductors and Smart Materials), DMF and NMP solvents, LiP_8 intermediates and black phosphorous (2D semiconductors). The instrument resolution is 0.1 ppb. No Co, Cr and Mn are detected within this limit. Based on the magnetisation per unit mass of Fe (the highest trace magnetic impurity) 217.6 emu/g, 9.2×10^{-8} g of Fe would be required to produce our observed SQUID signal. This corresponds to 97.8 ppb. The amount of Fe we detect is well below this amount. This suggests our SQUID results cannot be explained by any magnetic impurities.

Supplementary Note 4: Additional discussion of EPR data

The first set of cwEPR measurements were carried out on Setup 1 (see **Experimental methods**) as this allowed for higher sensitivity, using the high-quality factor (Q-factor) Bruker ER 4122-SHQE resonator. It also allowed for field monitoring using a Bruker ER 035 M NMR Gaussmeter along with calibration using a standard - N@C60 sample with a well-known g-factor of 2.00204 (Ref 1).

We find that at room temperature there exists a broad $g \approx 2$ signal, which confirms the presence of unpaired electrons in the inner wall PNR thin film sample. We carry out an orientation study by rotating around the long axis of the EPR tube. In a homogenous sample, there should not be any orientation dependence to the EPR signal. However, it was clear by eye that the inner wall film was highly inhomogeneous with different thicknesses. This is confirmed *via* EPR where we see a strong dependency to both the *g*-factor and peak to peak linewidth (lwpp) as a function of rotation. We rotate the sample tube though 360° in steps of 10° and find the maximum *g*-factor of ≈ 2.20/2.21 is reached at angles $\theta \approx 40°$, 130° (repeating at 220°, 310°) and a minimum *g*-factor of 2.03 at 80° (repeating at 260°). The maximum determined *g*-factor of 2.20-2.21 is in line with the calculated out-of-plane *g*-factor for bilayer/2 layer (2L) back phosphorous[2]. While the minimum *g*-factor determined to be 2.03 is in line with the calculated in-plane *g*-factor (in-plane *g*-factor is not considered to have a layer dependent *g*-factor). Finally examining the angle dependence of the *g*-factor we clearly see that most data points are around the 2.1-2.15 value, and 2.14 is the calculated out-of-plane g-factor for monolayer black phosphorus. Hence, the $g \approx 2$ EPR signal occurs due to predominantly mono- and bi-layers of PNRs and not a greater number of layers.

θ (°)	*g*-factor	Lorentzian lwpp (mT)
0	2.1239	13.5
10	2.1451	17.9
20	2.1603	19.0
30	2.2070	19.4
40	2.2127	17.4
50	2.1267	17.7
60	2.0670	14.7
70	2.0403	13.6
80	2.0291	14.0
90	2.0411	13.5
100	2.0884	12.1
110	2.1424	13.9
120	2.1901	14.9
130	2.1998	13.0
140	2.1747	13.4
150	2.1361	12.5
160	2.0983	12.6
170	2.0962	11.8
180	2.1182	12.5
190	2.1382	17.6

200	2.1550	19.5
210	2.1910	17.5
220	2.2110	13.5
230	2.1276	18.6
240	2.0702	14.3
250	2.0436	11.8
260	2.0350	13.0
270	2.0426	12.9
280	2.0838	11.9
290	2.1412	14.2
300	2.1914	13.3
310	2.2018	14.2
320	2.1782	14.6
330	2.1382	13.0
340	2.0996	12.5
350	2.1014	12.0
360	2.1260	13.5

Table S2: Extracted *g*-factor and linewidth of the $g \approx 2$ EPR signal as a function of rotation angle at room temperature.

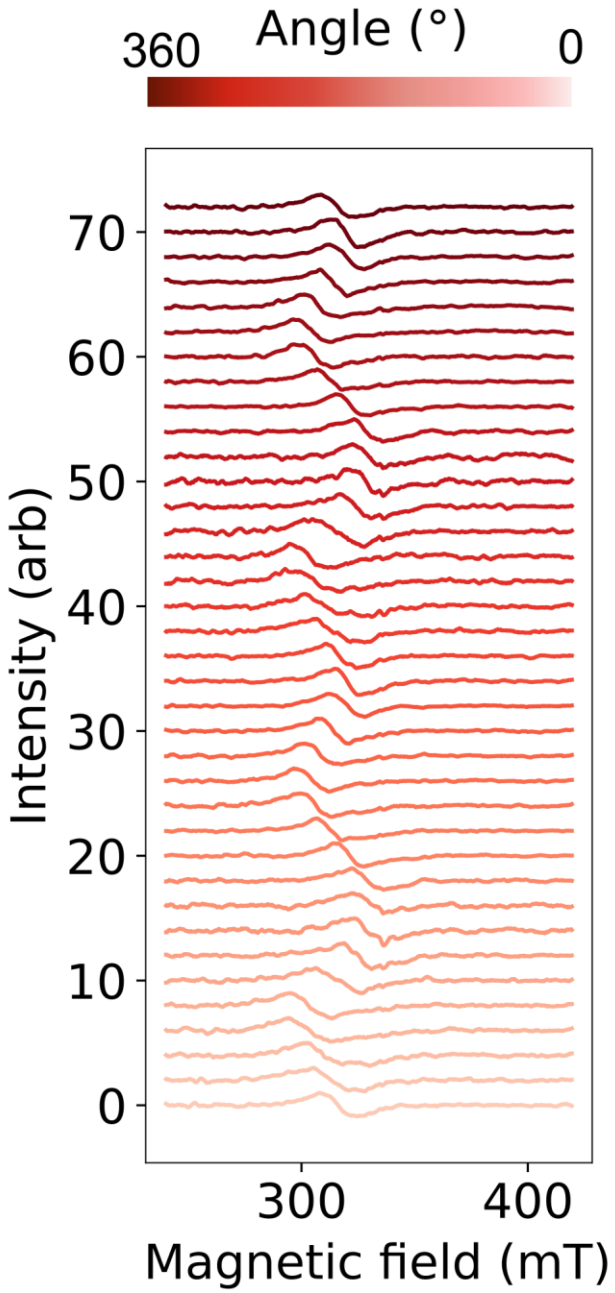

Fig. S5: $g \approx 2$ EPR signal as a function of rotation angle at room temperature (FMR-like signal/slope removed).

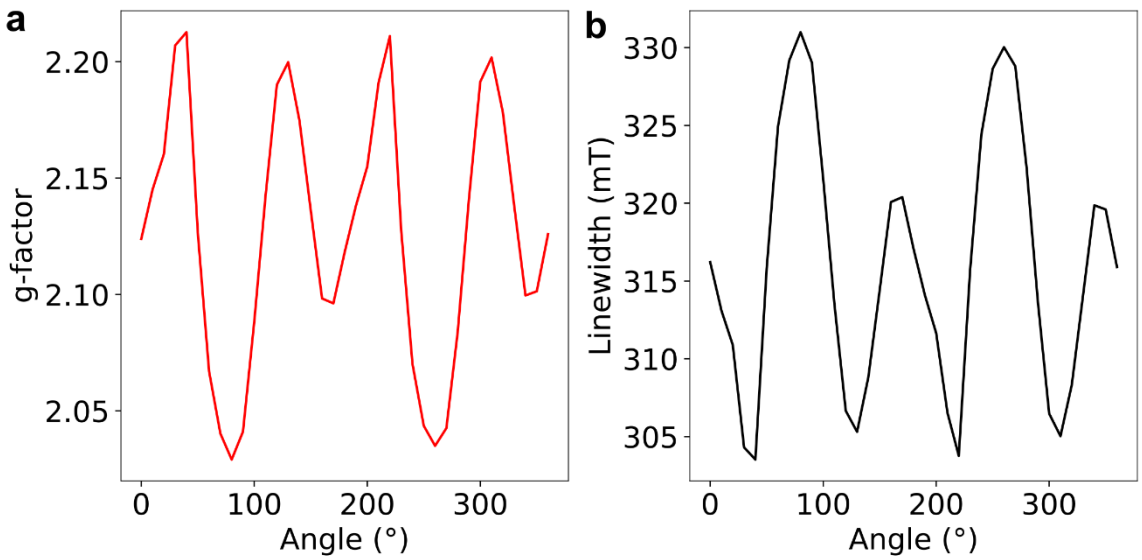

Fig. S6: Extracted *g*-factor and linewidth of the *g*≈2 EPR signal as a function of rotation angle at room temperature.

Next, we investigate the cwEPR spectrum as a function of lowering temperature, from 296 K to 15 K by sitting at an angle of θ ≈ 100° (see **Main Text Figure 2c**). At θ ≈ 100° the *g*-factor is 2.0908, not too far off the out-of-plane mono layer value but far-off from the in-plane value. Most crucially however, at this angle the linewidth is the narrowest, which gives the best opportunity to see changes in the cwEPR spectra as a function of decreasing temperature.

We see that θ ≈ 100°, lowering the temperature from 296 K down to 195 K, leads to an increasing *g*-factor from 2.0908 to 2.1124 and an increasing lwpp from 12.3 mT to 13.9 mT. From 195 K to 75 K the *g*-factor sees the reverse behavior where it decreases from 2.1124 to 2.0567, while the linewidth remains much broader than at 296 K. The *g*-factor increases from 75 K to 65 K before vanishing between 55-40 K. The disappearance of the signal and the increased linewidth either side of this 55-40 K range is in line with observations of a phase transition, around this temperature range, as seen in the SQUID measurements. At 35 K the signal reappears with a *g*-factor of 2.0464 and continues to increase until 15 K reaching 2.0563. The sharper signal which does not change with orientation but is more prominent at lower temperature is a background signal from the resonator cavity. A finer temperature study is underway, which will be part of a future publication.

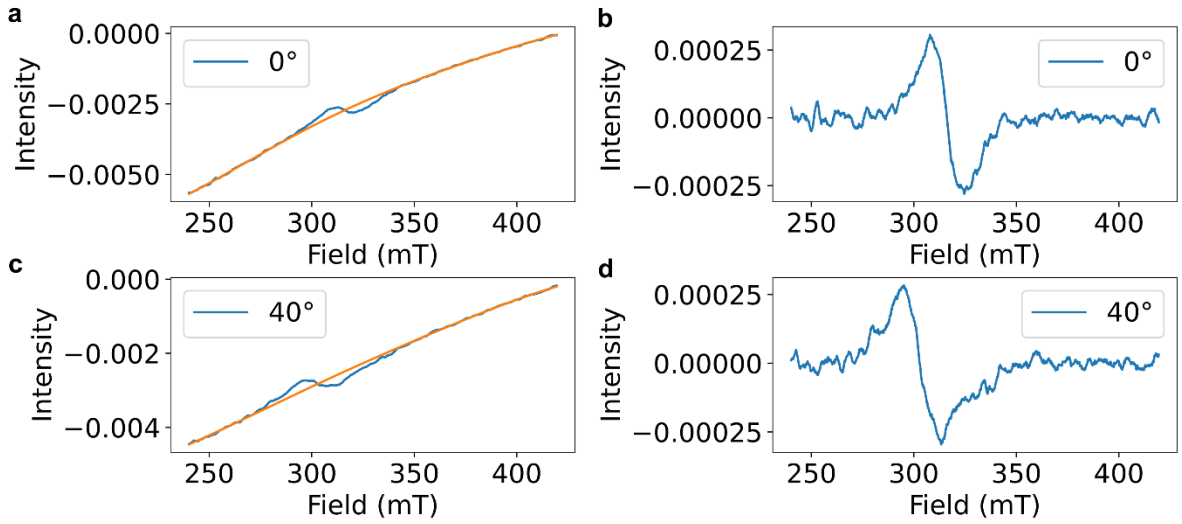

Fig. S7: Background subtraction of EPR data: **a-b.** Raw signal, polynomial fit (a) and corrected signal (b) at 0°. **c-d.** Raw signal, polynomial fit (a) and corrected signal (b) at 40°.

In all the raw narrow scan cwEPR spectra there is a slope which corresponds to the FMR like signal (which also has a strong orientation dependency). In order to determine the *g*-factor, lwpp and to clearly see the trend in the EPR signal we removed the FMR like signal's slope using a suitable polynomial fit. An example of the raw signal, polynomial fit and corrected signal is given in **Figure S7** for angles denoted 0° and 40°. Similar processing was carried out on all narrow scan cwEPR spectra (rotation study and temperature series) to only show the $g \approx 2$ EPR signal.

Next, we move to Setup 2 (see **Experimental methods**), which allows for broader magnetic field scans going from 6 mT to 1.45 T. This board magnetic field range means field calibration is not possible however we do not expect any field offset to be more than 0.4 mT. The wide scan reveals additional signals, apart from the $g \approx 2$ EPR signal, which are much more intense and even broader. We attribute these to ferromagnetic resonance (FMR) signals which most likely result from domains where there is strong interactions between the PNR layers. The FMR like signals exhibit a strong orientation dependency, however, there seems to be more than one domain contributing, with some signals significantly changing with sample tube rotation and some not changing considerably. While the analysis of the FMR like signals is increased in complexity by the inner wall film and its inhomogeneity, we attempt to show the possible behavior of different domains by fitting the data at each angle with four derivatives signals. Three corresponding to the FMR like signals (two purely Lorentzian and one Voigtian component) and one purely Lorentzian derivative for the $g \approx 2$ EPR signal.

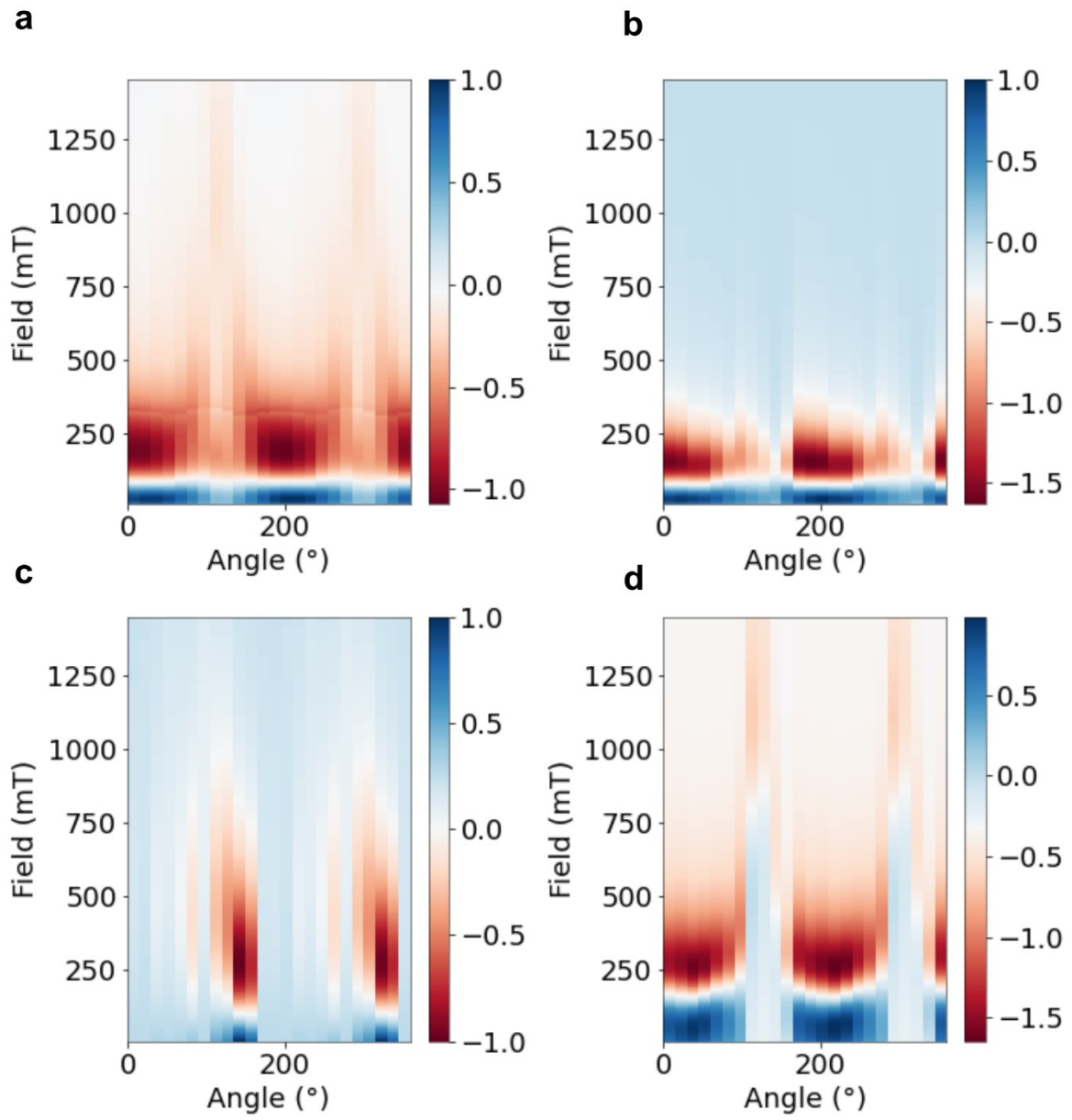

Fig. S8: Fitting of EPR data: a. Wide field EPR scan as a function of angle. **b-c.** Decomposition of EPR wide-field range scan into signals 1, 2 and 3 respectively as detailed in text.

We fit the spectrum at each angle to give a coarse understanding of the magnitude and distribution of internal fields in different domains of PNR present in the inner wall film that give rise to the FMR like signal. We see that the experimental data can be modelled well with these four derivative signals. We observe that two signals (signal 1 and 2) remain centered at fields <100 mT (one pure Lorentzian and one Voigtian component), while one signal (signal 3 pure Lorentzian component) shows large shifts with orientation of the sample tube (see **Figure S8**).

We determine the net internal field of signals 1 and 2 to be ≈225-265 mT by taking the difference between the field corresponding to the $g \approx 2$ signal and the center of signals 1 and 2. Since the effective resonance position of signals 1 and 2 is at lower magnetic fields compared to a $g=2$ signal (which would have negligible internal fields) the net internal fields for these domains must be aligned to the external magnetic field direction. Signals 1 and 2 have large linewidths most likely reflecting the large distribution of internal fields. We suggest that the effective resonance positions of signals 1 and 2 do not change significantly with orientation as these PNRs are being easily (re-)magnetized.

In signal 3 the net internal fields are determined by taking the difference between the maximum and minimum effective resonance positions. Since the effective resonance position changes from around 850 mT to 240 mT we estimate the net internal field to be ≈600mT. The linewidth of signal 3 is also broad again suggesting a wide distribution of internal fields. We suggest that the effective resonance positions of signal 3 changing significantly with orientation could be due to these PNRs being hard to (re-)magnetize. This results in the FMR signal at ≈850 mT when the net internal field is anti-aligned to the external magnetic field direction, while the FMR signal at ≈240 mT is due to the net internal field being aligned (or close to aligned) to the external magnetic field direction.

We speculate that the difference in the behavior of the FMR signals which remain cantered at fields <100 mT at all orientations and the signal which shows strong shifts in its resonance field could be due to domains with easy and hard axes. However, the above analysis is simply to give an overview on the magnitudes of net internal fields and to show the presence of large distributions in internal fields present in this sample. The above analysis is not a unique fit or solution to the experimental data. Further measurements to understand the details of the FMR signals are ongoing.

The EPR and FMR like signals observed in this sample require further work to accurately characterize all properties, this work will form the basis of a future publication.

All fit to the EPR and FMR signals were carried out using the MATLAB toolbox EasySpin[3].

Supplementary Note 5: Temperature dependent Raman spectroscopy of PNRs

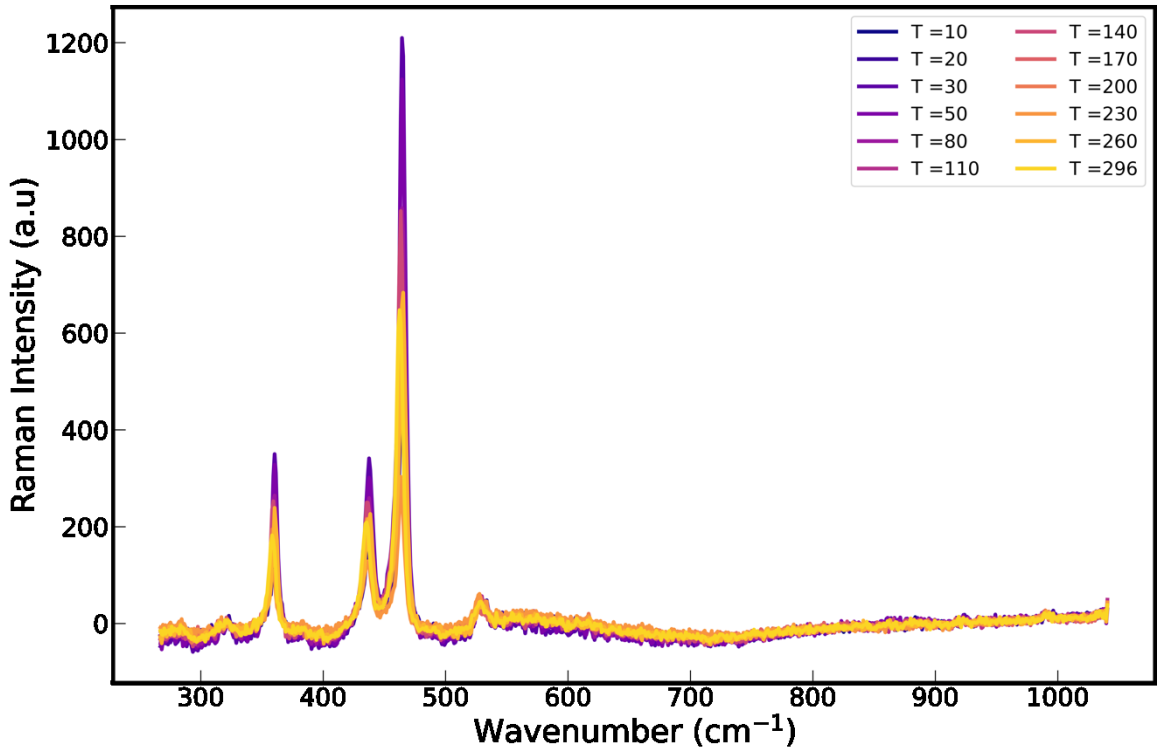

Fig. S9: Temperature Dependent Raman Microscopy of the PNRs: The Raman spectra of PNRs, down to 6K, show no extra features, consistent with no structural phase transition over this temperature range.

Supplementary Note 6: Temperature Dependent Absorption of PNRs

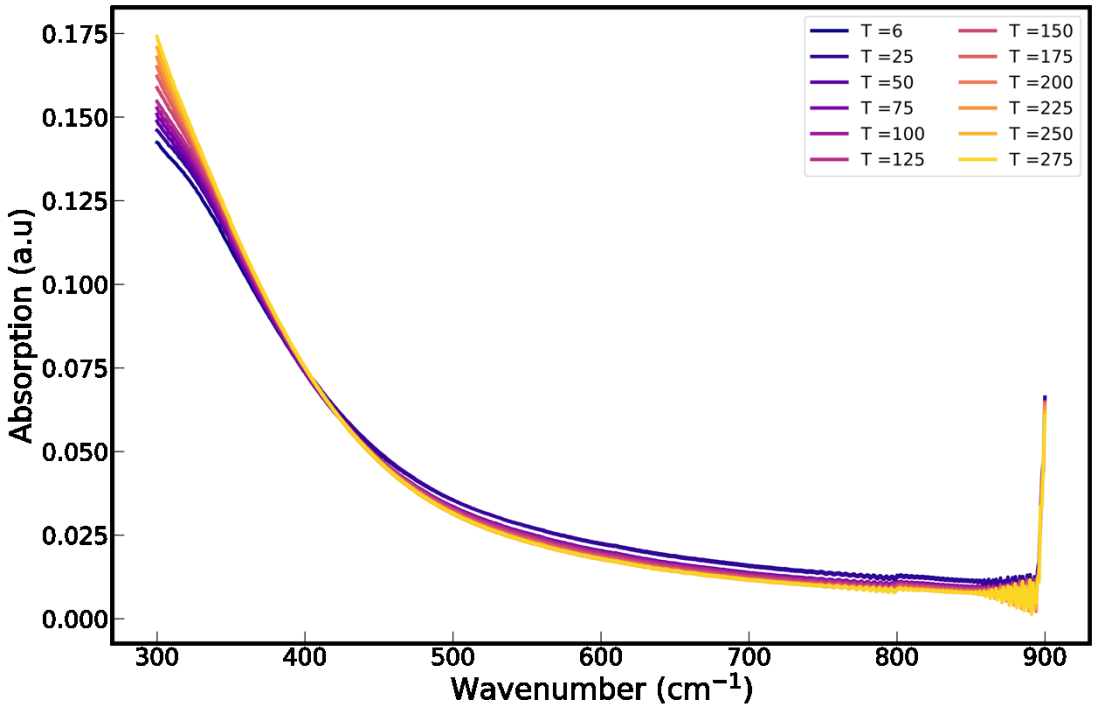

Fig. S10: Temperature Dependent Absorption of the PNRs: The absorption spectrum of the PNRs is broad and featureless down to 6K likely due to inhomogeneous broadening of absorption of the PNRs in solution.

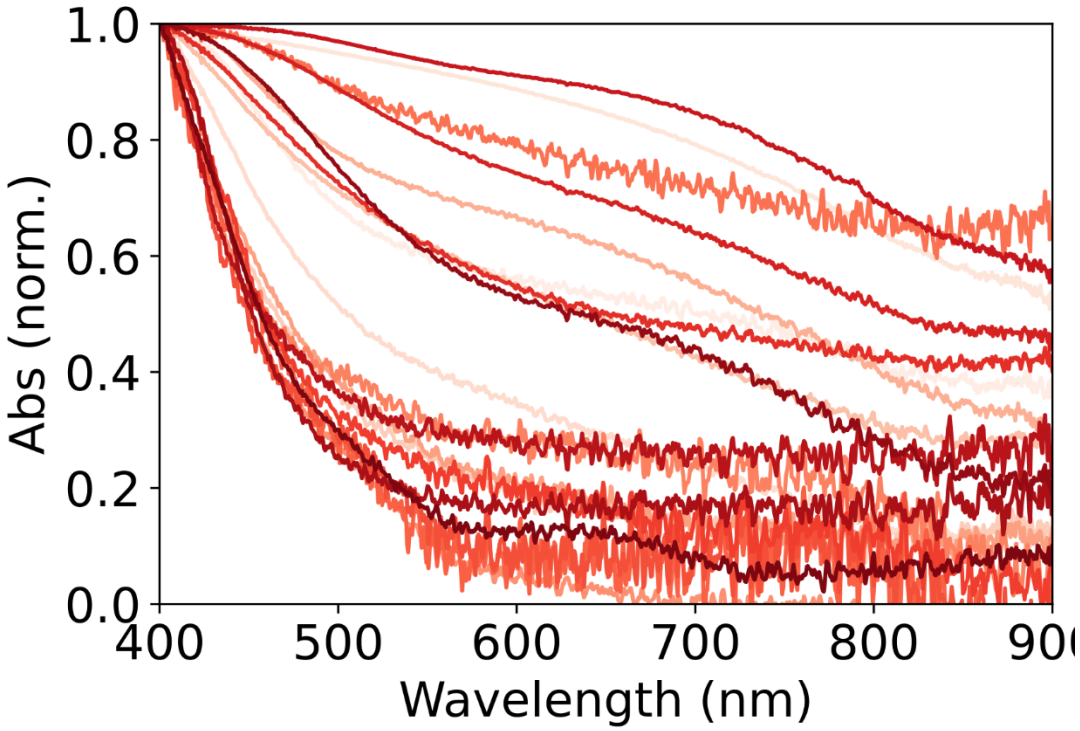

Fig. S11: Absorption spectrum of individual PNRs: Absorption spectroscopy of individual (large) PNRs was performed on a customised Zeiss Axio microscope with illumination provided by a halogen lamp (Zeiss HAL100). Transmitted light was collected using a 50×/0.4 objective (Nikon, T Plan SLWD) and spatially filtered using a 100 µm-diameter optical fibre (Avantes FC-UV100-2-SR) mounted in confocal configuration and connected to a spectrometer (Avantes AvaSpec-HS2048). PNR samples were prepared *via* drop-casting from solution onto cleaned (Acetone/IPA) 0.17 mm thick glass slides. The absorption spectrum is broad and featureless regardless of ribbon but a large degree of variation is observed between ribbons in-line with the inhomogeneity observed in rotation of the inner wall sample in EPR.

Supplementary Note 7: Scaling of pump-probe signal with magnetic field

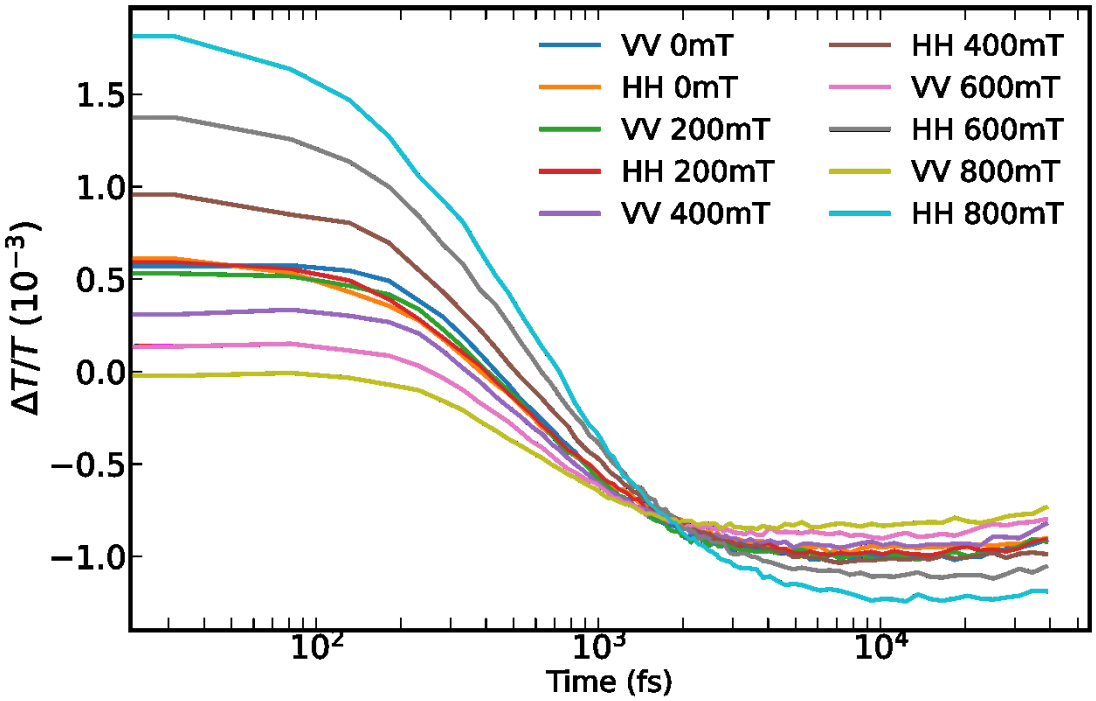

Fig. S12: Magnetic Field Dependence of the Pump-probe signal: At intermediate fields from those shown in the main text (200,400 and 600 mT), the splitting between the HH and VV signal linearly increases as would be expected based on the linear dichroism results shown in Figure 1 of the main text.

Supplementary Note 8: Impulsive Raman spectra

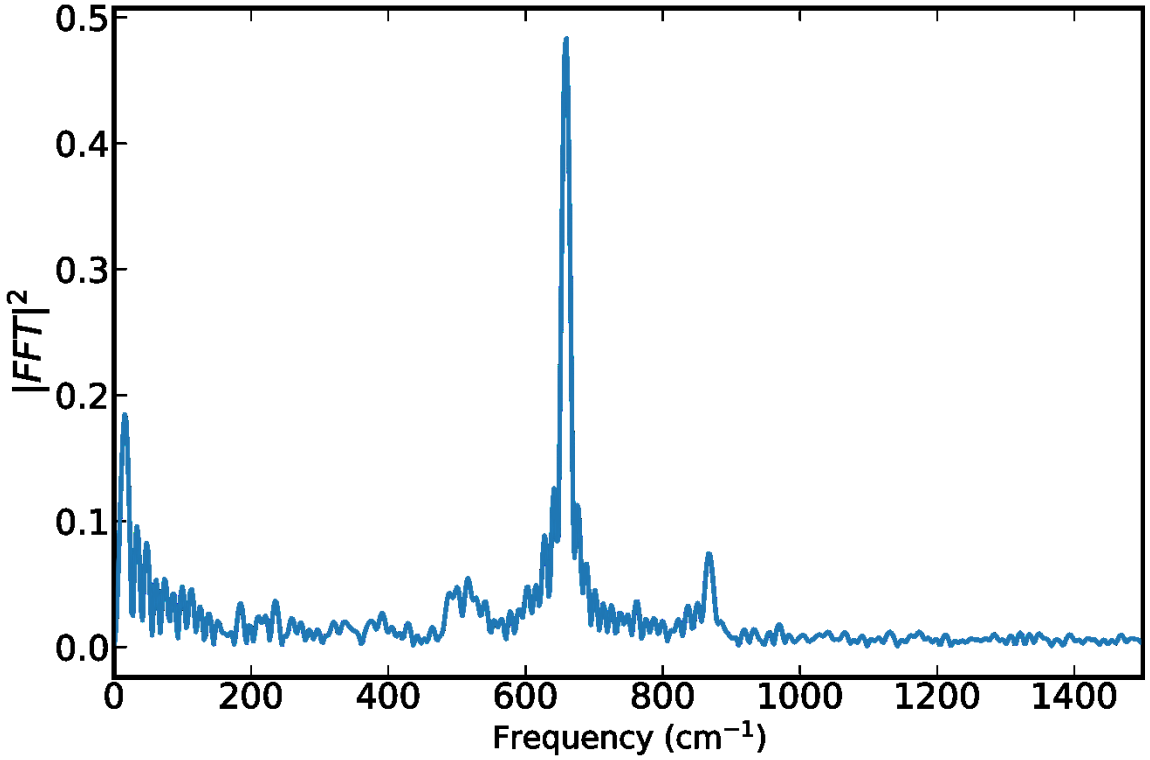

Fig. S13: Off-resonant Impulsive Vibrational Spectroscopy of PNRs in DMF: The off-resonant broadband pump pulse on the PNR solution from 700-800 nm does not show the edge phonon mode coupling as compared to the resonant pulse (500-600 nm) shown in the main text Figure 4. This is further evidence for the coupling of the edge phonon to the excited state of the PNRs.

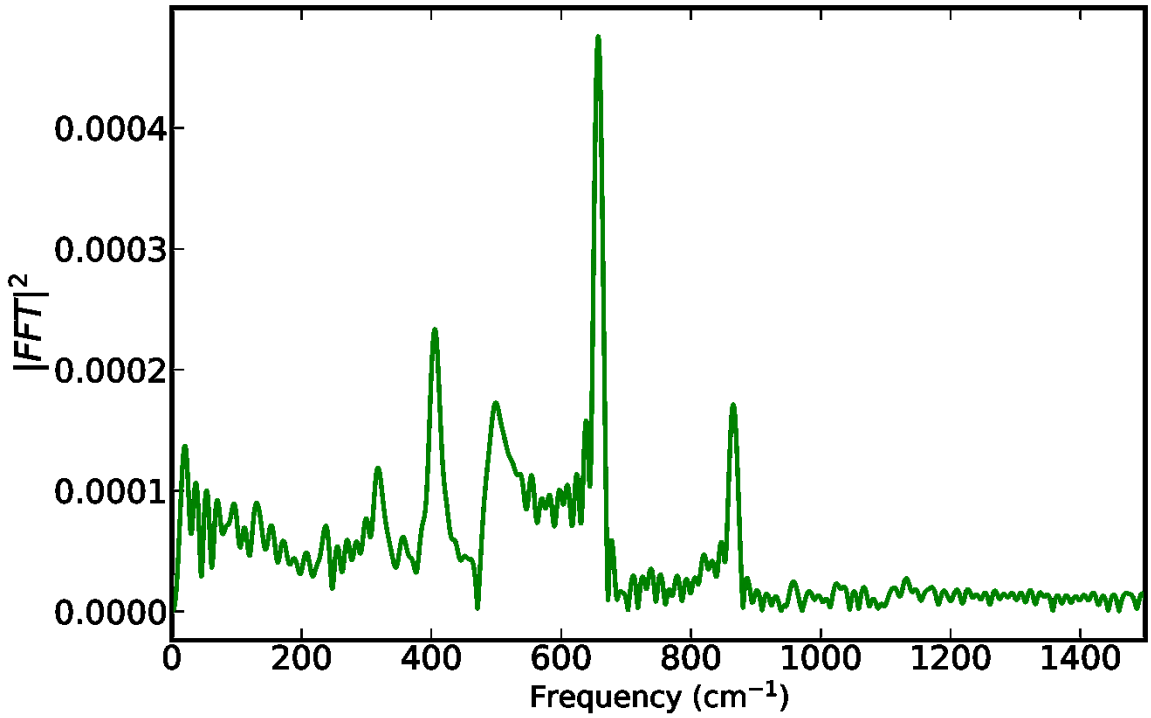

Fig. S14: Impulsive Vibrational Spectroscopy of pure DMF: The same resonant broadband pump pulse used on the PNR solution (500-600 nm) is used to study a pure DMF solution to ensure the phonon mode we ascribe to the PNR edge is not arising from the solvent. As can be seen, this mode is not present in the pure DMF solvent. This confirms that is indeed arising from the PNRs.

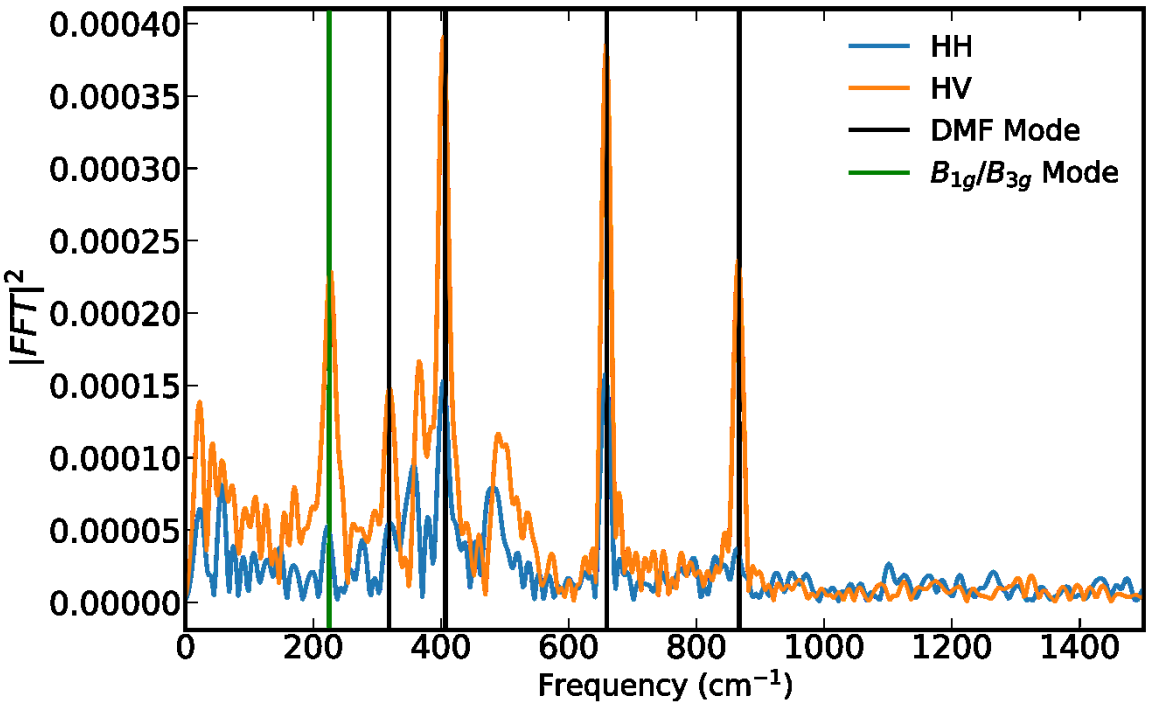

Fig. S15: Polarisation Dependent Impulsive Vibrational Spectroscopy of the edge mode: The edge phonon mode (green line) is only present when studying the impulsive vibrational spectrum in the orthogonally polarized pump-probe configuration suggesting that the vibration selectively couples to the diploe polarized along the ribbon's long axis.

References

1. Wittmann, J. J. *et al.* High-precision measurement of the electron spin g factor of trapped atomic nitrogen in the endohedral fullerene N@C60. *J. Magn. Reson.* **290**, 12–17 (2018).
2. Zhou, X. *et al.* Effective g factor in black phosphorus thin films. *Phys. Rev. B* **95**, 1–8 (2017).
3. Stoll, S. & Schweiger, A. EasySpin, a comprehensive software package for spectral simulation and analysis in EPR. *J. Magn. Reson.* **178**, 42–55 (2006).